Soft Matter

Dynamic Article Links

Cite this: *Soft Matter*, 2012, **8**, 10950

www.rsc.org/softmatter

PAPER

Alignment and dynamics of elongated cylinders under shear

Sandra Wegner,*[a] Tamás Börzsönyi,[b] Tomasz Bien,[c] Georg Rose[c] and Ralf Stannarius[a]

Received 22nd June 2012, Accepted 15th August 2012
DOI: 10.1039/c2sm26452h

When a granular material consisting of macroscopic elongated grains is exposed to shear, the individual grains align. We determine the particle distribution functions and orientational order parameters and study the collective dynamics as well as individual particle motion during shearing. X-ray computed tomography (CT) is used to obtain three-dimensional images of the shear zone. All individual particle positions and orientations are extracted by image processing software and the complete order tensor is determined. We compare the behavior of our ensembles of macroscopic grains with well-known continuum models for shear alignment and director dynamics of anisotropic liquids. Irrespective of the completely different particle interactions and size scales, analogies are found even on a quantitative level. Measurements of the local packing densities inside and outside the shear zone reveal a shear dilatancy, irrespective of the more efficient packing that can be expected for ordered ensembles of cylinders compared to randomly oriented samples.

1. Introduction

Shape-anisotropic particles in large ensembles can be found on all length scales in everyday life, from mesogenic molecules, rod-shaped viruses, bacteria or anisotropic colloids to rice grains or beans and other elongated seeds. Technical products with elongated particle shapes range from micrometer glass rods, screws, nails and wooden pegs to tree trunks in logjams on rivers. The individual constituents are sometimes immersed in a liquid, *e.g.* in aqueous solution. Depending upon the materials, sizes and the interstitial fluids, their interactions can be very different, *e.g.* van der Waals forces and electric dipolar interactions, hydrodynamic forces, or hard-core steric repulsion. Irrespective of the huge variety of these systems, some characteristic phenomena can be observed on all levels. Among these phenomena is the tendency to exhibit local orientational order, and the tendency to align in a preferred direction, when exposed to shear stress.

The best investigated and most comprehensively understood systems of shape-anisotropic entities that show orientational order and shear alignment are molecular liquid crystals. A mean field model (Maier–Saupe model) has been developed that describes the formation of orientational order in the nematic phase. It proved extremely successful,[1] for example in the modeling of the nematic–isotropic phase transition. Macroscopic properties of the fluid can be described by equations for the local director $\boldsymbol{n}$ (preferential direction of the mesogens). A continuum description has been developed for the viscous and elastic forces acting on the director (Leslie–Ericksen equations[2]). These equations predict a variety of phenomena in the director dynamics, and they are well confirmed by numerous experiments. Among these predictions is the alignment of $\boldsymbol{n}$ with a small angle respective to the streamlines when the liquid crystal is exposed to shear flow. This alignment can be quantitatively related to material parameters (see below). Recently, it has been demonstrated quantitatively[3] that the elongated cylinder or ellipsoid shaped macroscopic particles exhibit shear alignment in some analogy to nematic liquid-crystalline materials.

Nematic phases are formed not only by molecular constituents. On a microscopic level, one finds mesophases of elongated nano-crystallites or nano-rods in suspensions,[4–10] viruses like TMV[11–13] and fd,[14,15] or bacteria.[16,17] Clay platelets in aqueous solutions[18,19] are nanoparticles that can form lyotropic nematic or smectic mesophases. It is well known that they show shear-alignment as well, but often such observations have been described only qualitatively (see *e.g.* ref. 11).

The practical consequences of such an alignment are manifold. For example, shear stresses depend upon order and alignment in the shear region. This has to be considered whenever elongated or flattened grains are processed in food or pharmaceutical industries. On the other hand, shear-aligned structures can provide evidence of flow processes. In geophysics, imbrication is the well-known phenomenon of orientational order of elongated deposit materials.[20,21] Oriented clasts, which can be compared to a run of toppled dominoes, build a depositional fabric. From the alignment of such shape-anisotropic volcaniclastic mass-flow deposits, one can conclude on the flow patterns during active deposition phases.

[a]*Otto-von-Guericke Universität Magdeburg, Institute for Experimental Physics, D-39016 Magdeburg, Germany. E-mail: sandra.wegner@ovgu.de*
[b]*Institute for Solid State Physics and Optics, Wigner Research Center for Physics, Hungarian Academy of Sciences, P.O. Box 49, H-1525 Budapest, Hungary*
[c]*Otto-von-Guericke Universität Magdeburg, Chair for Medical Engineering and Healthcare Telematics, D-39016 Magdeburg, Germany*

In this study, small pegs (diameter of a few millimeters) serve as models for particles with hard-core interactions. The particles are in direct contact with each other, they interact sterically. This distinguishes them from diluted systems where the individual particles also interact *via* an embedding fluid (such situations are described, for example, in ref. 22 and 23). Under shear flow, orientational order and alignment are exhibited. Astonishingly, the effects are comparable to the director behavior in molecular nematics, even on a quantitative level.

The paper is organized as follows: in the next section, we describe the experimental setup and introduce the X-ray CT method for the non-invasive three-dimensional imaging of grain positions and orientations in the sheared granular bed. We shortly recollect the basic equations for the characterization of the state of order and orientation. Then, we characterize the shear zone geometry, and determine the parameters describing order and alignment of the anisometric grains in the bulk and at the free surface of the shear zone. We compare the collective dynamics of the sheared granulate with the individual particle dynamics. A comparison with the director dynamics of low molecular mass nematic liquid crystals is made. Finally, we discuss the influence of shear flow on the packing of the cylindrical particles.

2. Experimental

The experiments are performed with wooden pegs of three different aspect ratios $Q = L/D$. They will be shortly denoted as Q5 (length $L = 25$ mm, diameter $D = 5$ mm, aspect ratio $Q = 5$), Q3 ($L = 20$ mm, $D = 6$ mm, $Q = 3.3$) and Q2 ($L = 10$ mm, $D = 5$ mm, $Q = 2$). They are shown in Fig. 1b–d. The shape of the Q2 species is exactly cylindrical, whereas the shape of the other two species is between that of cylinders and spherocylinders, as their ends are tapered. The surface of the Q3 pegs and part of the Q5 and Q2 pegs has slight groves. The choice of these objects was basically motivated by practical reasons. We did not find a measurable influence of the surface properties in the experiments.

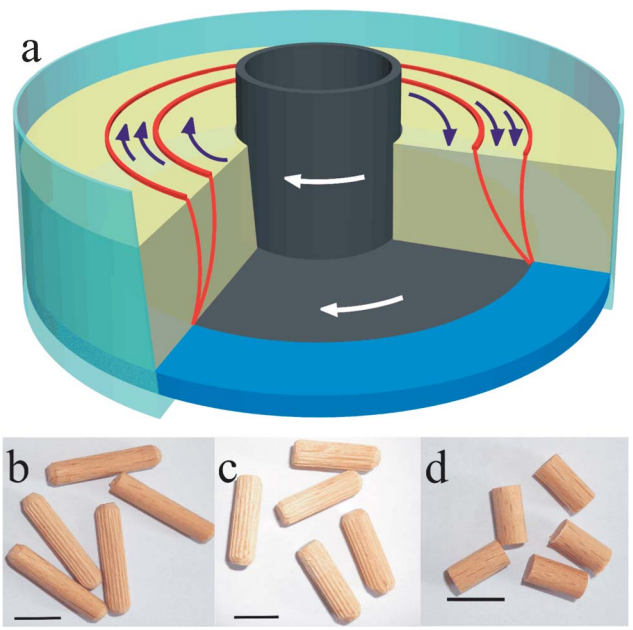

Fig. 1 (a) Schematic illustration of the split bottom shear cell, dark gray (online: red) curves in the bulk indicate the shear zone. (b–d) Photographs of particles studied, pegs with aspect ratios $Q = L/D$ of (b) 5, (c) 3.3 and (d) 2. The horizontal bars correspond to 1 cm.

Order parameters and particle orientations are analyzed in a cylindrical shear container geometry. The experimental setup is shown in Fig. 1a. The container has an outer radius of 28.5 cm, and a fill height of 5 cm to 6.5 cm. The bottom disk with radius 19.5 cm is connected to an inner cylinder with radius 8 cm. We shear the granular material by rotating the inner part (the small inner cylinder and the thin bottom disk), as illustrated by the white arrows. The strain is localized in the so-called shear zone, which is indicated by red (dark grey) lines in the figure. After some rotation of the inner part of the cell, the shear zone is formed and the preferred orientation of particles in this zone develops. The radius of the shear zone is roughly equal to the radius of the bottom disk, *i.e.* large with respect to the particle dimensions.

There are different options for the observation of the particles under shear. First, the arrangement of grains can be detected using CT. These data can be analyzed separately at different locations in the granular bed, at the surface, in the bulk far from the container boundaries, and near the container walls. We employ a medical X-ray angiography machine (Siemens Artis zeego) at the INKA lab, Otto von Guericke University, Magdeburg. It consists of a rotational C-arm based X-ray source mounted on a high-precision robot-arm with a flat-panel detector featuring high resolution whole volume computer tomography scanning. The spatial resolutions chosen were 2.03 pixels per mm and 1.48 pixels per mm, respectively. The corresponding recorded volumes were 25.2 cm × 25.2 cm × 19 cm and 34.8 cm × 34.8 cm × 24.4 cm, respectively.

After ten full rotations of the inner part of the shear container, when we can be sure that all transients have vanished, the first image is recorded. In order to obtain a good statistics of particle positions and orientations, a series of independent scans is taken after further rotations. Between subsequent scans, the central part of the granulate is rotated by approximately 180°, so that the particle positions in the shear zone can be considered independent in subsequent scans. More than 130 measurements were performed for each grain type. For the particle tracking experiments discussed in Section 4.2, smaller rotation steps were used.

Exemplarily, a horizontal slice of an X-ray CT image is shown in Fig. 2a. The borders of the shear zone are marked by dashed lines. The slice is 2 cm below the free surface of the material and it corresponds to the white-bordered area shown in Fig. 2b (the top view of the split-bottom container). The particles in the recorded volume are detected by conversion of the images to binary data and by application of a watershed algorithm. Each individual particle orientation was computed from the inertia tensor of the respective detected object. The principal axis of inertia with the smallest eigenvalue defines the orientation $\vec{\ell}$. The sense of orientation is irrelevant here. Because the particles are apolar, we consider $\vec{\ell}$ and $-\vec{\ell}$ equivalent.

Fig. 3 visualizes an arrangement of the cylinders in the sample, as computed from the analysis of one typical tomogram. We show the cross-sections of the granular bed vertical to the flow lines (a) and horizontal across the shear zone (c), where the detected particles are represented by cylinders and visualized by a ray tracing algorithm.

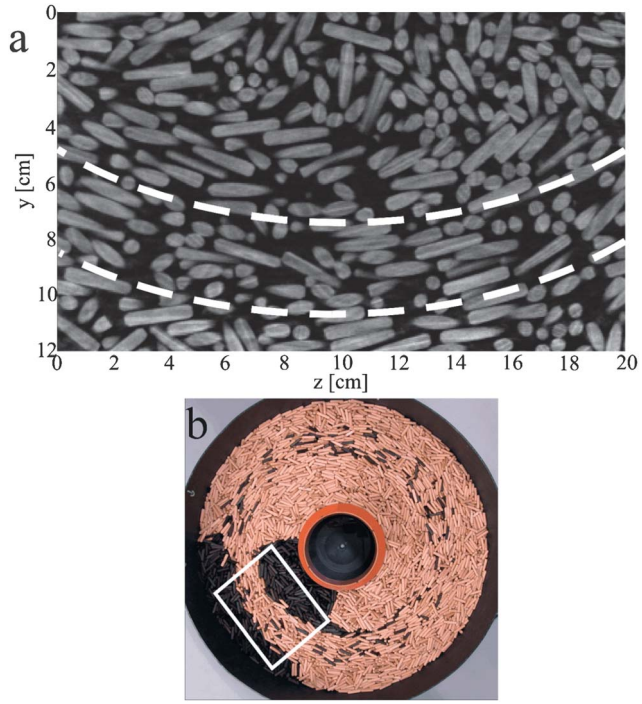

Fig. 2 CT image: (a) one slice of a CT image taken at a position shown in (b) 2 cm under the surface, dashed white lines indicate the borders of the shear zone.

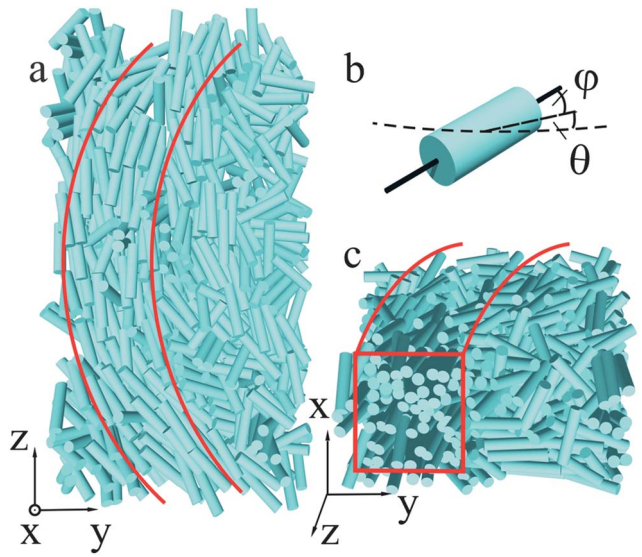

Fig. 3 Visualization of the distribution and orientation of particles in the granular bed. The images are reconstructed from the particle positions and angles computed from the tomogram (see text) by a ray-tracing program. (a) Top view of the granular bed at approximately half of its total depth, the upper particles are hidden, (b) definition of the alignment angle θ and tilt angle φ, (c) vertical cut through the shear zone, normal to the streamlines, the front particles are removed. Lines (red) sketch the shear zone limits.

In the further data evaluation, we distinguish between particles in a surface region of ≈ 1 cm depth (two particle diameters) and bulk particles in a 2 cm thick layer below this region. The data collected in each series of experimental images correspond to between 10 000 and 20 000 particle positions for the surface and bulk regions, respectively. The idea of this somewhat arbitrary discrimination is to check whether there are differences between the order of bulk particles and particles in the surface layer. Surface data can be collected alternatively with less expensive optical observation techniques.[3] The comparison of X-ray surface and bulk data provides an estimate of how representative the optical surface analysis is for the shear alignment in the bulk.

From the orientation of the individual particles, order and alignment data are derived numerically. The shear-induced orientational order is monitored by diagonalization of the symmetric traceless order tensor $\boldsymbol{T}$:

$$T_{ij} = \frac{3}{2N}\sum_{n=1}^{N}\left[\ell_i^{(n)}\ell_j^{(n)} - \frac{1}{3}\delta_{ij}\right], \qquad (1)$$

where $\vec{\ell}^{\,(n)}$ is the unit vector along the long axis of particle n, and the sum is over all N detected particles. The largest eigenvalue of $\boldsymbol{T}$ is the primary order parameter S. A second, biaxial order parameter D is defined as the difference of the two other eigenvalues of $\boldsymbol{T}$. In addition to the principal values of this tensor, the directions of its principal axes contain the information on the shear alignment. Therefore we analyze the orientation of these axes relative to the local shear flow. The local alignment can be characterized by two quantities: the shear alignment angle θ_a is measured between the principal axis of $\boldsymbol{T}$ corresponding to the largest eigenvalue S and the local tangent. It measures the deviation of the preferential orientation of the grain long axes from the streamlines. We use a second angle φ_a, between the principal axis of the largest eigenvalue of $\boldsymbol{T}$ and a horizontal plane, to characterize the mean direction of the particles in a plane normal to the shear gradient. In a truly two-dimensional shear geometry, it would be reasonable to conclude from symmetry considerations that the average of this second angle should be zero, *i.e.* the nose-up and nose-down orientations of sheared particles should be equivalent. In practice, our shear geometry is somewhat asymmetric, the shear zone broadens from bottom to top (see below), but the effect on φ_a is negligible. We note that the angles θ and φ (Fig. 3b) are not Euler angles, they have been introduced here only for a convenient description. Because of the particle symmetry (ℓ and $-\ell$ are indistinguishable), orientations (θ_a, φ_a) and ($\theta_a + \pi$, $-\varphi_a$) are equivalent, therefore we restricted the parameter range of θ_a to $[-\pi/2, \pi/2]$.

3. Model

Before we consider the experimental results, we shortly discuss the meaning of the calculated order parameters and alignment angles in our experiments.

In contrast to the previously mentioned microscopic systems, where interactions between individual constituents are of the order of thermal energy, thermal motion is negligible for particles of millimeter sizes and above. The consequence is that liquid crystalline phases cannot be expected there, the material needs continuous energy supply to be fluidized. Ordered states are created by shear or other agitation, and they remain preserved after preparation.

In thermotropic liquid crystals, the order tensor describes the average orientation of the mesogen axes. In a nematic phase

formed by calamitic (rod-like) mesogens, it refers to the preferred average orientation of the molecular long axes. The individual molecules perform fast motions (in the Gigahertz region) around the local director. The nematic order parameter is a thermodynamic quantity. Its value is primarily a function of temperature, its dependence on shear flows or director dynamics is often negligibly small. This is different in suspensions of microscopic shape-anisotropic particles where the effect of induced order can reach noticeable magnitudes. In the macroscopic granulate systems considered here, there is no 'natural' order parameter, the local state of order depends upon the previous treatment of the sample. A random arrangement of particle axes is possible, but often the preparation steps (filling, pouring, and shaking) result in a non-zero local orientational order (*e.g.* ref. 24 and 25). Some frozen-in short range order in local domains can hardly be avoided in freshly prepared samples of elongated grains. Starting with such a configuration, a well defined orientational order and a clear alignment form under shear, independent of the previous state.

In nematic liquid crystals, the continuum (Leslie–Ericksen) equations provide a mathematical model for flow alignment, they describe the reorientation of the director in an inhomogeneous flow field. If we assume for simplicity that the director stays in the plane formed by shear gradient and flow ($\cos\varphi \approx 1$), the viscous torque balance yields an equation of motion[26]

$$\dot{\theta} = C\left(\sin^2\theta - \frac{\alpha_3}{\alpha_2}\cos^2\theta\right) \tag{2}$$

with θ describing the angle between the director and the flow direction. The equilibrium solutions are

$$\theta = \pm\theta_a = \pm\arctan\sqrt{\frac{\alpha_3}{\alpha_2}},$$

α_2 and α_3 represent nematic viscosity coefficients. The negative coefficient C contains material and flow field parameters. The coefficient α_2 is negative, its absolute value is often very close to the rotational viscosity $\gamma_1 = \alpha_3 - \alpha_2$. In most calamitic nematics, α_3 is also negative and much smaller than α_2, which results in the stable shear alignment angle θ_a and an unstable equilibrium at $-\theta_a$. One can rewrite eqn (2) to

$$\dot{\theta} = C\left(1 - \frac{\cos^2\theta}{\cos^2\theta_a}\right). \tag{3}$$

The shear rate does not enter the equation for the stationary angle θ_a (but it is contained in C). In some nematics, particularly in the vicinity of the transition to smectic phases, α_3 can become positive. Then, there is no stable shear alignment angle of the director (tumbling regime).

In the granular material, which shows comparable shear alignment properties, it is tempting to compare not only the equilibrium angle, but also the dynamics of individual grains with the dynamic eqn (2) for the nematic director. However, one has to be aware that these two systems represent physically completely different situations. The analogue of the director dynamics is the collective motion of an ensemble of grains which are initially oriented in a given direction to the flow, rather than the individual particle dynamics. These details are discussed below.

The differential equation (3) for the director reorientation has two solutions:

$$\theta = \arctan(\tan\theta_a \tanh(\theta_a Ct)) \tag{4}$$

and

$$\theta = \arctan\left(\tan\theta_a \frac{1}{\tanh(\tan\theta_a Ct)}\right). \tag{5}$$

Both are plotted in Fig. 4 exemplarily for an alignment angle of $\theta_a = 7°$. The first solution (solid line) describes the case when the initial angle is in the range of $-\theta_a < \theta(0) < \theta_a$, the second solution (dashed line) is for $|\theta(0)| > \theta_a$. In both cases the director finally reaches the stable fixed point, in the first case the shortest reorientation path is chosen, while in the latter case the director performs an almost complete half rotation.

When the dynamic equation of the nematic continuum model, eqn (2), is applied to the granular experiment discussed here, one has to replace the time derivative by an appropriate substitute, *viz.* the shear strain γ of the granulate plays the role of time in eqn (4) and (5). In our experiment, the relevant parameter is basically the number of neighboring particles that pass a given grain in the shear zone and exert torques by direct contact, $\tilde{C}\gamma$ replaces Ct in the equations for the reorientation dynamics.

4. Results

4.1 Order, orientation and collective dynamics

Initially, the geometry of the shear zone was analyzed for each material by excavation. The container was filled with colored pegs in a sector of approximately 75°. The inner part of the split-bottom container was rotated several turns, thereby the particles in the shear zone were spread as shown in Fig. 5a–c. The pattern of dark grains shows the width of the shear zone in the top layer. Then the granulate was carefully removed layer by layer, as seen in Fig. 5d–f. The shear zone can be clearly distinguished from the non-sheared parts by the distribution of colored particles in each layer. The analysis of these images yields the graph of the shear zone profile as shown in Fig. 5g. The shear zone has a width of several particle lengths, it widens towards the free surface of the granulate. Compared with previous shear measurements with

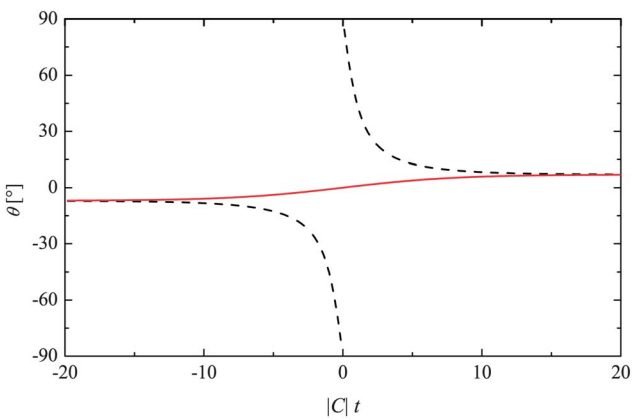

Fig. 4 Dynamics of the angle between director and shear direction θ for nematic liquid crystals for $\theta_a = 7°$. The solutions are 180° periodic.

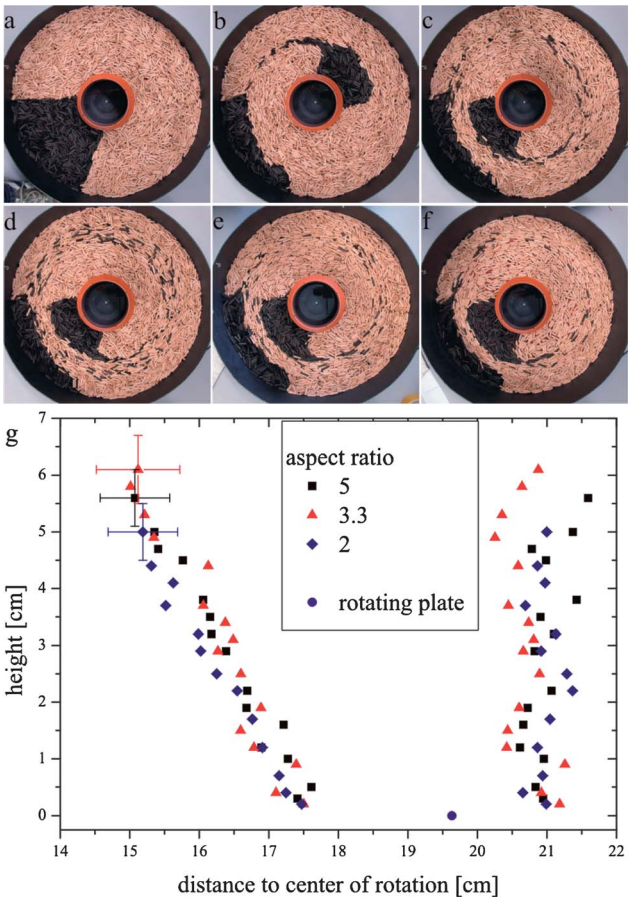

Fig. 5 Excavation of the shear cell with pegs with the aspect ratio 5. (a–c) Photographs of the top layer after 0, 0.5 and 3 rotations (d–f) during excavation, at heights 4.3 cm, 3.0 cm and 0.5 cm. (g) Geometry of the shear zone for the 3 different aspect ratios, error bars in the left upper corner are representative for all data of the respective series.

other materials,[27,28] the zone is unusually wide at the bottom of the shear cell. Probably this has to be attributed to the geometry of the bottom disk, whose edge is about 5 mm (one particle diameter) higher than the bottom of the container. The zone is approximately five particle diameters wide at the bottom, irrespective of the aspect ratio. It reaches about twice that width in the upper part of the granular bed. We will distinguish in the evaluation between the complete shear zone and a core zone of 1.3 cm width in its center.

The measured distributions of the orientation angles of particles in the shear zone are shown in Fig. 6 and 7. These distributions have been determined separately for particles at the surface (a layer thickness of 1 cm was chosen as a compromise between a sufficiently large ensemble of particles and satisfactory resolution) and particles in the bulk, sufficiently far from both the container walls and the free surface (1 cm to 3 cm from the top). Another presentation of the same data is shown in the insets, comparable polar plots are commonly used *e.g.* for geological data. Each distribution shows a maximum. The graphs in Fig. 6a show the angular distribution in the horizontal plane. The error in these graphs of about 5% originates mainly from the statistical uncertainty (ensembles of about 10^4 particles are evaluated). The first moment of this distribution gives the

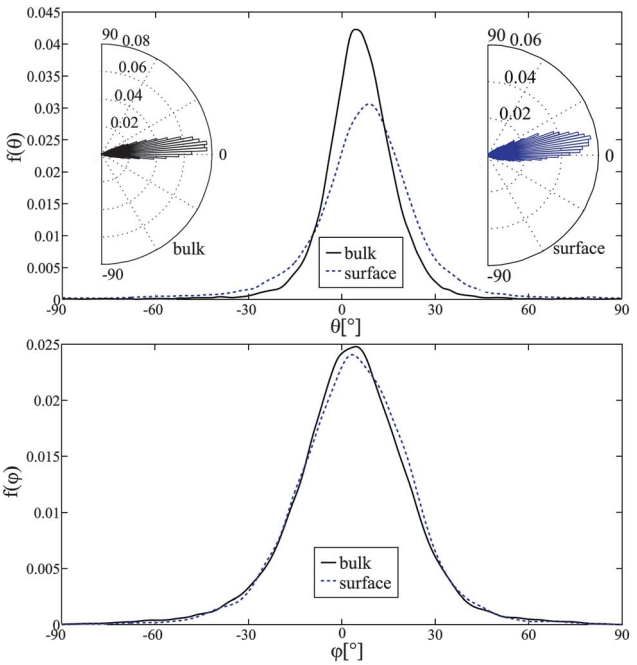

Fig. 6 Distributions (a) of the angles θ in the horizontal plane respective to the local tangent, and (b) φ vertically with respect to the horizontal plane, for pegs with $Q = 5$. Black (solid) and blue (dashed) curves correspond to the bulk and surface zones, resp. Since the particles are symmetric, orientations θ and $\theta \pm 180°$ are equivalent, thus it suffices to plot the distributions in the interval $-90° \leq \theta \leq 90°$, the same applies to φ. Insets in (a) show the distributions of θ in polar diagrams.

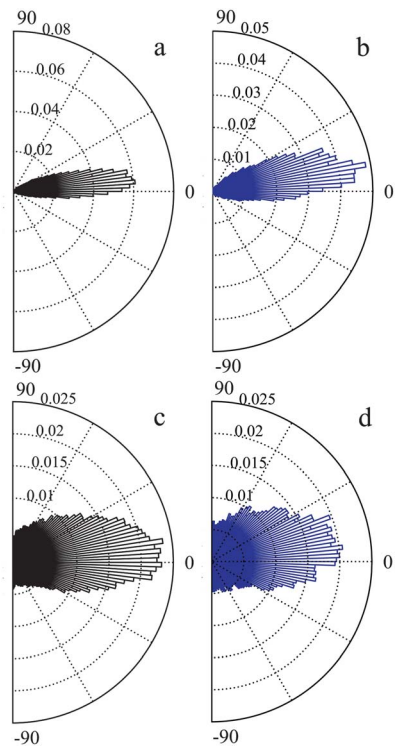

Fig. 7 Same as in Fig. 6a, distribution of the angle θ in the bulk (a and c) and in the surface layer (b and d) for the shorter pegs Q3 (a and b) and Q2 (c and d).

shear alignment angle. Since the distribution is nearly symmetric, this angle is practically identical to the maximum of the distribution. The majority of particles in the shear zone has only small deviations from the preferred orientation. Statistical results are compiled in Table 1. Particles with smaller aspect ratios are less ordered, *i.e.* the standard deviations of both distributions are higher. Their alignment angle θ_a is larger. The biaxial order parameter increases with decreasing aspect ratio Q. The eigenvector with the second largest eigenvalue of the order tensor is roughly normal to both flow direction and shear gradient, while the eigenvector with the smallest eigenvalue forms an angle of θ_a with the shear gradient. This means that fluctuations of the particle long axes are more probable in the direction perpendicular to flow and shear gradient. This can be understood intuitively since the alignment is achieved primarily by torques that cause reorientations within the shear plane.

Comparing the bulk and surface values, one finds the primary order parameter always slightly smaller at the surface than in the bulk. The alignment angle is somewhat larger. Nevertheless, the qualitative results and the trends of order and alignment with the aspect ratio are very similar in bulk and surface regions. The distribution functions of the vertical angle are similar as well. We find a very small non-zero average tilt φ_a, which is much smaller than the distribution width, *i.e.* at the limits of experimental uncertainty. However, the deviations seem to be systematic (slightly positive in all experiments). Comparing the core of the shear zone with the data from its full width, one finds almost equal results. This evidences that the stationary alignment is not shear rate dependent, as expected.

Table 1 Data for particles with different aspect ratios for different parts of the shear cell. Last column gives data for a part outside of the shear zone with distance $R = 11$ cm to 13 cm from the center of rotation. The last row gives the number of particles analyzed

Height (mm)	10–30	10–30	0–10 surface	10–30
Zone	Shear zone full width	Shear zone core	Shear zone full width	Outside
Pegs Q5 with aspect ratio 5				
S	0.81	0.81	0.76	0.24
D	0.09	0.09	0.03	0.12
θ_a	6.9°	6.3°	9.1°	14.8°
σ_θ	12.8°	12.9°	18.6°	42.0°
φ_a	3.6°	2.8°	4.5°	0.4°
σ_φ	19.1°	19.2°	18.4°	35.9°
No. of particles	27 447	11 817	8527	10 188
Pegs Q3 with aspect ratio 3.3				
S	0.72	0.72	0.68	0.39
D	0.12	0.12	0.05	0.16
θ_a	8.0°	8.0°	10.8°	15.6°
σ_θ	17.8°	18.2°	21.2°	40.8°
φ_a	3.3°	3.1°	3.1°	5.8°
σ_φ	23.3°	23.4°	21.7°	25.1°
No. of particles	30 450	13 384	8677	9979
Pegs Q2 with aspect ratio 2				
S	0.27	0.27	0.20	0.09
D	0.21	0.21	0.19	0.06
θ_a	10.1°	10.1°	13.4°	7.1°
σ_θ	38.1°	38.1°	41.1°	49.6°
φ_a	5.4°	5.1°	3.2°	7.1°
σ_φ	37.8°	37.9°	38.6°	35.7°
No. of particles	68 241	29 247	28 329	30 519

Outside of the shear zone, the particle distributions are not perfectly random, which can be seen from the non-zero local order parameter. The locally ordered domains are randomly distributed. This is the consequence of the container filling procedure, which cannot guarantee an absolutely random particle distribution (see, *e.g.* ref. 24 and 25).

The formation of order, *i.e.* the quantitative initial evolution of three quantities of interest, the primary order parameter S, the mean angle θ_a in the horizontal plane and the standard deviation σ_θ were analyzed in two types of experiments. The first experiment starts with freshly filled 'randomly' oriented pegs. The results are shown in the left hand graphs of Fig. 8. Each graph was constructed in the following way: the CT image of the sample was recorded, then the inner container part was rotated by a small angle (corresponding to a displacement of about 1 cm across the shear zone) before the next image was taken. The time evolutions were constructed from about 150 to 200 CT images each. Because the statistics is now only over all particles in a single image (130 to 380 depending upon the particle sizes), the experimental uncertainty is much larger than in Fig. 6 and Table 1. Therefore, the fluctuations at late stages are purely statistical. All graphs start from a low order parameter related to the filling procedure. Then, the order parameter increases and it quickly approaches an asymptotic value, after about 10 cm displacement of the circumference of the bottom disk ($\gamma \approx 2.5$). The alignment angle is established somewhat slower. Its initial value is arbitrary, the shear alignment angle θ_a adjusts after $\gamma \approx 5$. This value is independent of the shear rate in our

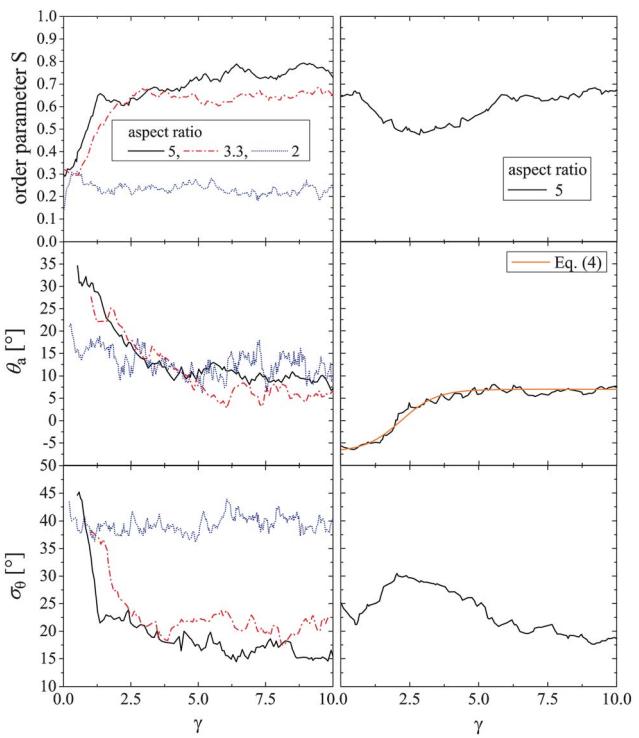

Fig. 8 Evolution of order parameter S, average angle in the horizontal plane θ_a and its standard deviation σ_θ for two different initial conditions, left: randomly oriented particles after fresh filling, right: change of the shear direction of an aligned sample. The smooth (orange) line in the θ_a graph in the right column represents eqn (4) with $\tilde{C} = 6.2$.

experiments, it gives a rough measure of the deformation needed to align the sheared particles. Each particle has to pass about 3 to 5 neighbors before the stable alignment angle is approached. In the materials with larger aspect ratio, an initial fast decay of σ_θ is evident.

The second experiment started from a well defined initial configuration. First we prepared a shear-aligned configuration. Then, the rotation direction was reversed. This experiment was performed with the Q5 pegs. One expects that the order parameter drops when the particles realign towards the new, mirrored shear alignment angle, while the width of the distribution of θ will temporarily increase. The gradual reorientation of the alignment angle θ can in principle occur in two ways, either by almost a half rotation of the grains, starting away from the flow direction, or by a short reorientation passing the flow direction (*cf.* Fig. 4). The experimental results are seen in the right hand graphs of Fig. 8. All three observed quantities evolve towards their new stationary values within an average strain of $\gamma \approx 6, \ldots, 7$. This behavior is verified by surface measurements with digital optical imaging. After reversion of the direction of shear, the transient is about twice as long as the evolution of alignment from random initial conditions. The evolution of the average alignment angle in Fig. 8d follows qualitatively the solution (4) of eqn (2), corresponding to the solid line in Fig. 4, with the parameter $\tilde{C} = 6.2$.

4.2 Individual particle dynamics

Under constant shearing, one finds occasional reorientations of individual particles by almost a half rotation, similar to the dashed curve in Fig. 4. We track individual pegs in order to characterize such reorientations. Almost all of them rotate in the same direction, $\dot{\theta} < 0$, as given in eqn (2). Rotating particles first have a negative angle to the flow direction, which decreases up to a perpendicular orientation ($-90°$) and then decreases further from 90° (which is equivalent to $-90°$) towards the alignment angle θ_a. Examples of such rotations are plotted in Fig. 9. During the initial transient, almost all particles reach the equilibrium angle by such rotations. The trajectories of individual grains are not smooth, since the rotation is driven by collisions with neighboring particles. On the right hand side of Fig. 9, typical trajectories have been superimposed. The dashed line is the solution of eqn (5) with the same $\tilde{C}$ as shown in Fig. 8. It is not astonishing that, while the collective dynamics of the grain orientation average is reasonably well described by an equation analogous to that for nematic director dynamics, the coincidence of single grain dynamics with the latter is only superficial. A more detailed analysis of individual particle dynamics will be achieved from optical studies of elongated grains at the surface of the granular bed (method introduced in ref. 3). In these less intricate and less expensive optical measurements, a better statistics can be expected.

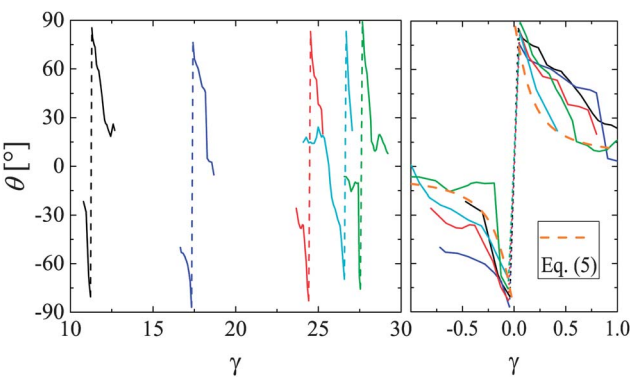

Fig. 9 Typical reorientations of particles after perturbations from the shear aligned state. The trajectories are measured in units of the shear strain (tangential displacement of the center of the shear zone). The right hand graph shows some typical trajectories superimposed, and the dashed line indicates the solution of eqn (2) with the same parameter $\tilde{C}$ as in Fig. 8.

4.3 Reynolds dilatancy

Shear of regular grains has multiple effects on local packing. Already in spherical grains, partial crystallization can lead to states with higher local packing.[29] Ellipsoidal particles that are partially aligned by shear or by other effects are partially aligned and show a tendency to increase their packing.[30] For rod-like particles, one may expect an even larger effect of orientational order on the packing efficiency, a perfectly orientation-ordered system of rods may achieve densities near the random close packing of 2D disks. On the other hand, there is a well known tendency of dense granular matter to expand in flow, a phenomenon known as Reynolds dilatancy. In the system of sheared granular rods, both effects counteract in the shear zone and they compensate each other partially.

In a similar experimental shear geometry as used here, Sakaie *et al.*[28] have reported a decrease of the packing fraction in sheared spherical grains by about 15%. We have calculated the packing fraction for the Q3 particles from CT images. The two-dimensional plot in Fig. 10 is a cross-section perpendicular to the shear flow direction, the abscissa is along the radial coordinate in the container. Outside the shear zone the packing density is approximately 0.65. At the bottom of the container, one can see some regular stratification pattern owing to some boundary-induced ordering of the rods (about 2–3 layers). Inside the shear zone, the relative decrease of packing fraction is about 12%. The drop of packing density is rather sharp towards the outer boundary of the shear zone. At the top of the granular bed, boundary effects penetrate into the granular bed no deeper than approximately one particle diameter. It is characteristic for all measurements that the upper surface of the granulate shows a

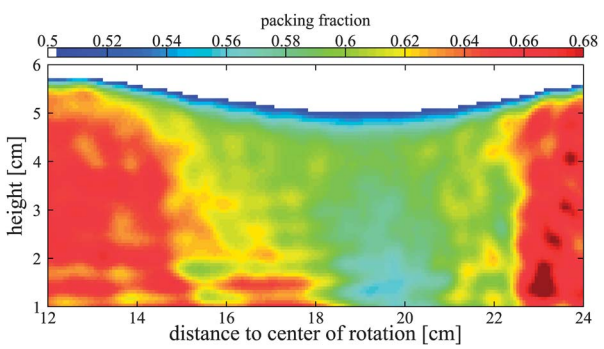

Fig. 10 Packing density of the Q3 pegs across the shear zone.

certain depletion above the shear zone, even though the packing density in the region below is smaller than in the initial granulate.

Obviously, the Reynolds dilatancy is qualitatively the dominant phenomenon, and the resulting decrease in packing fraction is similar to that observed for poppy seeds.[28] The order parameter is obviously too low for a compaction of the aligned rods to take noticeable effect. Note, that all our CT measurements (as well as the MRI measurements by Sakaie *et al.*[28]) have been carried out on the system at rest, between shearing steps. We do not exclude that during continuous shear the packing fraction becomes even lower, and at the end of each shearing step gravity helps the system relax towards a denser configuration.

5. Summary and conclusions

In this study we investigated the shear induced alignment of anisometric granulates in a bulk sample using X-ray computed tomography. In the cylindrical container the shear zone had practically the same shape and width for all three samples with $L/D = 2$, 3.3 and 5. In the shear zone, particles align and on average form a small angle with the streamlines. This angle decreases with increasing aspect ratio. In addition, the standard deviations of the measured angles in the shear plane and perpendicular to it decrease. This corresponds to a growing order parameter with increasing aspect ratio. The material in the core of the shear zone and the material in the complete shear zone width give similar results for numerous quantities including the order parameter, alignment angle, and biaxiality. This indicates the shear rate independence of the phenomenon. There is a slight tendency towards an increasing order parameter and decreasing shear alignment angle with increasing aspect ratios of the grains, at a given grain shape (*e.g.* spherocylinders).

The stationary alignment state is reached from a random sample after the material is sheared by approximately 4 to 5 times the shear zone width (rotation of the inner disk by approximately 60°). The displacement across the shear zone corresponds to 30 to 40 particle diameters for all investigated samples. In a configuration where the initial alignment in the shear zone is at $-\theta_a$, *i.e.* after a reversal of the shear direction, the new stationary state is reached after approximately twice as long time. The mean orientation angle of the particles follows a path from $-\theta_a$ to θ_a that is very similar to eqn (4).

Tracking the time evolution of particle orientations revealed that almost all particles in orientations $|\theta| > \theta_a$ reorient in the same direction. Also, during the transient from the disordered state nearly all particles reorient in the same sense towards θ_a. This is a similarity to nematic liquid crystals. However, for particles deviating from the alignment angle in the range $-\theta_a < \theta < \theta_a$, both directions of rotation are observed, with a slight excess to negative $\dot{\theta}$, in contrast to the nematic director solution, eqn (4).

Summarizing, the dynamics of individual grains as well as the dynamics of the ensemble average have been investigated experimentally in a sheared granulate composed of anisometric particles. We find shear induced orientational order in the shear zone, and we measure the alignment of the particle long axes. Many features are similar to the director dynamics in nematic liquid crystals, even though the underlying physics appears to be completely different. As in the low molecular mass liquid crystals, the characteristics of the stationary alignment is independent of the shear rate. The shear rate only sets the time scale for the formation of the ordered state.

Differences between the granular system and the molecular mesophases lie in the nature of the orientational order, which is induced by agitation in the former system, and a thermodynamic quantity in the latter. Differences are also found in the dynamics. The director equations describe qualitatively the evolution of the shear alignment angle of the granulate, particularly under flow reversal. The individual particle dynamics of the grains is much more complex.

The packing density of the elongated particles in the sheared regions is influenced by two counteracting effects. The classical dilatancy of granulates under shear which tends to reduce the packing fraction is partially compensated by the tendency of the partially ordered cylinders to pack closer. In the sum of both effects, the dilatancy dominates, the packing fraction decreases by approximately 12% in the sheared region.

Acknowledgements

The authors acknowledge the Inka Lab of Otto von Guericke University Magdeburg for the opportunity to use the X-ray tomography facilities (funded by the BMBF, reference no. 03IP710). Financial support from the DAAD-MÖB researcher exchange program no. 29480 is acknowledged.

References

1 G. R. Luckhurst and C. Zannoni, *Nature*, 1977, **267**, 412.
2 F. M. Leslie, *Q. J. Mech. Appl. Math.*, 1966, **19**, 357.
3 T. Börzsönyi, B. Szabó, G. Törös, S. Wegner, J. Török, E. Somfai, T. Bien and R. Stannarius, *Phys. Rev. Lett.*, 2012, **108**, 228302.
4 A. H. W. W. Song and I. A. Kinloch, *Science*, 2003, **302**, 1363.
5 D. C. A. Dessombz, P. Davidson, P. Panine, C. Chanéac and J.-P. Jolivet, *J. Am. Chem. Soc.*, 2007, **129**, 5904.
6 S. Meuer, K. Fischer, I. Mey, A. Janshoff, M. Schmidt and R. Zentel, *Macromolecules*, 2008, **41**, 7946.
7 M. Zorn, S. Meuer, M. N. Tahir, Y. Khalavka, C. Sönnichsen, W. Tremel and R. Zentel, *J. Mater. Chem.*, 2008, **18**, 3050.
8 S.-P. Sun, M. Wei, J. R. Olson and M. T. Shaw, *Rheol. Acta*, 2011, **50**, 65.
9 A. Eremin, R. Stannarius, S. Klein, J. Heuer and R. M. Richardson, *Adv. Funct. Mater.*, 2011, **21**, 556.
10 K. Kang, *Rev. Sci. Instrum.*, 2011, **82**, 053903.
11 F. C. Bawden, N. W. Pirie, J. D. Bernal and I. Fanhucken, *Nature*, 1936, **138**, 1051.
12 C. Wetter, *Biol. Unserer Zeit*, 1985, **15**, 81.
13 D. L. Hu, T. J. Goreau and J. W. M. Bush, *Exp. Fluids*, 2009, **46**, 477.
14 Z. Dogic and S. Fraden, *Phys. Rev. Lett.*, 1997, **78**, 2417.
15 E. Grelet, M. P. Lettinga, M. Bier, R. van Roij and P. van der Schoot, *J. Phys.: Condens. Matter*, 2008, **20**, 494213.
16 D. Volfson, S. Cookson, J. Hasty and L. S. Tsimring, *Proc. Natl. Acad. Sci. U. S. A.*, 2008, **105**, 15346.
17 W. Mather, O. Mondragón-Palomino, T. Danino, J. Hasty and L. S. Tsimring, *Phys. Rev. Lett.*, 2010, **104**, 208101.
18 L. J. Michot, I. Bihannic, S. Maddi, C. Baravian, P. Levitz and P. Davidson, *Langmuir*, 2008, **24**, 3127.
19 D. van der Beek, H. Reich, P. van der Schoot, M. Dijkstra, T. Schilling, R. Vink, M. Schmidt, R. van Roij and H. Lekkerkerker, *Phys. Rev. Lett.*, 2006, **97**, 087801.
20 D. Karátson, O. Sztanó and T. Telbisz, *J. Sediment. Res.*, 2002, **72**, 823.
21 N. W. Hayman, B. A. Housen, T. T. Cladouhos and K. Livi, *J. Geophys. Res., [Space Phys.]*, 2004, **109**, B05409.
22 H. J. Brenner, *Int. J. Multiphase Flow*, 1974, **1**, 195.
23 D. Gunes, R. Scirocco, J. Mewis and J. Vermant, *J. Non-Newtonian Fluid Mech.*, 2008, **155**, 39.

24 B. Buchalter and R. Bradley, *Phys. Rev. A: At., Mol., Opt. Phys.*, 1992, **46**, 3046–3056.
25 B. Buchalter and R. Bradley, *Europhys. Lett.*, 1994, **26**, 159–164.
26 I. W. Stewart, *The Static and Dynamic Continuum Theory of Liquid Crystals*, Taylor & Francis, London, New York, 2004.
27 T. Unger, J. Török, J. Kertész and D. E. Wolf, *Phys. Rev. Lett.*, 2004, **92**, 214301.
28 K. Sakaie, D. Fenistein, T. J. Carroll, M. van Hecke and P. Umbanhowar, *EPL*, 2008, **84**, 38001.
29 J.-C. Tsai and J. P. Gollub, *Phys. Rev. E: Stat., Nonlinear, Soft Matter Phys.*, 2004, **70**, 031303.
30 A. Donev, I. Cisse, D. Sachs, E. Variano, F. Stillinger, R. Connelly, S. Torquato and P. Chaikin, *Science*, 2004, **303**, 990–993.

